J. Fluid Mech. (2002), *vol.* 465, *pp.* 191–212.
DOI: 10.1017/S0022112002001039 Printed in the United Kingdom

Predictability of quasi-geostrophic turbulence

By WILLIAM J. MERRYFIELD AND GREG HOLLOWAY

Institute of Ocean Sciences, Sidney, BC, V8L 4B2, Canada
merryfieldw@pac.dfo-mpo.gc.ca

(Received 15 February 2001 and in revised form 21 February 2002)

A method is developed for statistical prediction of turbulent geophysical flows that is more efficient than ensemble integrations. We consider the evolution of low-order moments for inviscid quasi-geostrophic turbulence. Guided by statistical mechanics, equations are developed for predicting the mean and the variance about the mean as functions of position and time. These equations are consistent with the exact moment equations and contain irreversible (entropy producing) fluxes that must be specified in terms of known moments. Using simple choices for these dependences, the resulting scheme, involving just two spatial fields, typically outperforms 100-realization ensembles.

1. Introduction

Predictability of atmospheric and oceanic motions is fundamentally limited by a tendency for small differences in initial conditions to amplify: because measured initial conditions inevitably contain errors, prediction errors become large within a finite time. This is so even for prediction models that describe all relevant physical processes perfectly.

It is therefore vital that predictions include an indication of uncertainty. However, predictions based upon a single realization of initial conditions provide no such information. There are at least two means of obtaining estimates of forecast uncertainty. The first is to consider an ensemble of M sets of initial conditions, each compatible with observations, and to evolve each independently. Forecast uncertainty then can be estimated straightforwardly from ensemble statistics (e.g. Leith 1974; Stephenson & Doblas-Reyes 2000). An obvious drawback to this approach is its computational burden: many realizations are needed to obtain reliable statistics, despite advances in generating optimal initial conditions for ensembles (e.g. Houtekamer & Derome 1995).

A second means of obtaining forecast uncertainty is to consider equations for the evolving statistics themselves, an obvious choice for which is the low-order moments of the probability density function, or p.d.f. Because equations for moments of order n contain moments of order $n+1$, this approach leads to a closure problem. Like ensemble calculations, closure approximations such as the stochastic dynamics of Epstein (1969) and Fleming (1971) suffer high computational burden: for systems having N degrees of freedom, third-order moment closures require solving $O(N^2)$ equations and fourth-order closures $O(N^3)$ equations, each containing many terms.

The present paper seeks to develop more tractable means for statistical forecasting of first and second moments. Instead of applying a formal moment closure, we draw upon basic considerations from non-equilibrium statistical mechanics to obtain evolution equations for the mean and single-point variance field in terms of reversible

and irreversible (or entropy producing) fluxes. Entropy measures total uncertainty implied by the p.d.f. (e.g. Khinchin 1949; Shannon & Weaver 1949; Salmon 1998, Chap. 5), and is thus a natural measure of the information content of a probabilistic forecast. Carnevale & Holloway (1982) showed that under homogeneous inviscid dynamics, the entropy of pairs of realizations monotonically increases, meaning that the information content of forecasts from imperfect initial conditions monotonically decreases. The scheme developed here obeys a similar property.

The functional forms of the irreversible fluxes that appear in the moment equations must be specified, and using even a very simple model for these fluxes yields a scheme whose performance consistently exceeds that of ensemble forecasts using 100 realizations and can approach that of ensembles using 1000 realizations. The scheme is comparatively efficient because it evolves only two spatial fields, hence comprising $2N$ variables rather than MN variables as in the case of ensemble forecasts, or $O(N^2)$ and $O(N^3)$ variables as in the case of third- and fourth-order moment closures. A price for this efficiency is that the representation of forecast uncertainty is incomplete, consisting of spatial maps of the variances about the mean forecast fields, with no information about spatial correlations of forecast errors. Our formulation in a spatial rather than spectral domain (cf. Carnevale & Holloway 1982) is well suited to ocean models, in which irregular boundaries complicate the use of spectral methods and flow statistics tend to be spatially inhomogeneous.

In § 2 exact equations governing moment evolution for homogeneous quasi-geostrophic flow are formulated. The moment prediction method is developed in § 3 and discussed in the context of previous work in § 4. In § 5 its performance is compared to that of ensemble forecasts. Results are summarized and discussed in § 6.

2. Exact moment equations

Consider a representation of the ocean or atmosphere having N degrees of freedom. The instantaneous state of such a system corresponds to a point in N-dimensional phase space $(x_1 \ldots x_N)$. In the absence of perfect knowledge of such a state, the system can be described by the p.d.f. $p(x_1 \ldots x_N)$, and statistical information can be obtained by evaluating moments with respect to p.

In theory, the evolution of p is described by the Liouville equation (Gleeson 1970), but in practice this equation cannot be solved due to the large dimensionality of phase space. Alternatively, we can approximate p as the local density of an ensemble of M phase-space points, each representing an equally probable state of the system. The evolution of p can then approximated by evolving the ensemble. However, this requires updating NM quantities at each time step, which is impractical if N and M are large.

Alternatively, we consider equations governing ensemble statistics. We focus on the particular case of ideal unstratified quasi-geostrophic flow on an f-plane, a simple choice that isolates the inertial dynamics that limit geophysical flow predictability and has a known equilibrium p.d.f. The evolution of a single realization of potential vorticity q_i is governed by the barotropic potential vorticity equation,

$$\frac{\partial q_i}{\partial t} = -J(\psi_i, q_i), \tag{1}$$

where $q_i = \nabla^2 \psi_i + h$, ψ_i is single-realization streamfunction, $h = f(H_0 - H)/H_0$ is a measure of topographic height, where f is Coriolis parameter, H is depth, and H_0 is mean depth, and $J(\psi_i, q_i) = |\partial(\psi_i, q_i)/\partial(x, y)|$.

We consider the evolution of low-order moments of potential vorticity, in particular the mean

$$Q_1(\boldsymbol{x},t) = \frac{1}{M}\sum_{i=1}^{M} q_i(\boldsymbol{x},t) \equiv \bar{q}(\boldsymbol{x},t), \tag{2}$$

where overbars henceforth denote ensemble averages, and the single-point variance

$$Q_2(\boldsymbol{x},t) = \overline{[q(\boldsymbol{x},t) - Q_1(\boldsymbol{x},t)]^2}, \tag{3}$$

which we adopt as a measure of uncertainty.

To obtain an equation governing Q_1, we differentiate (2) with respect to time and substitute from (1). Writing $q_i = Q_1 + q_i'$, $\Psi + \psi_i'$ where Ψ is mean streamfunction, we obtain

$$\frac{\partial Q_1}{\partial t} = \underset{1A}{-J(\Psi, Q_1)} \underset{1B}{-\overline{J(\psi', q')}}, \tag{4}$$

where we have used $\overline{q'} = \overline{\psi'} = 0$. Mean Q_1 thus evolves according to term 1A describing advection of Q_1 by the mean velocity field, and term 1B that is quadratic in departures from the mean.

We obtain similarly an evolution equation for Q_2 by substituting (1) into the temporal derivative of (3), which yields

$$\frac{\partial Q_2}{\partial t} = \underset{2A}{-J(\Psi, Q_2)} \underset{2B}{-\overline{2q'J(\psi', Q_1)}} \underset{2C}{-\overline{J(\psi', q'^2)}}. \tag{5}$$

Term 2A describes advection of Q_2 by the mean velocity field. Term 2B is quadratic in departures from the mean, whereas term 2C is cubic. Uncertainty therefore remains zero if it vanishes initially.

It is straightforward to show that (4)–(5) conserve $Q_1^2 + Q_2$. Integrating (5) and $2Q_1$ times (4) over space and adding, we have

$$\frac{\partial}{\partial t}\int (Q_1^2 + Q_2)\,\mathrm{d}\boldsymbol{x} = -\int [J(\Psi, Q_1^2 + Q_2) + \overline{J(\psi', q'^2)} + 2Q_1\overline{J(\psi', q')} + 2\overline{q'J(\psi', Q_1)}]\,\mathrm{d}\boldsymbol{x} = 0, \tag{6}$$

because the first two terms on the right-hand side of (6) vanish, whereas the third and fourth terms cancel upon an integration by parts.

3. Moment prediction scheme

Solving moment equations (4)–(5) presents an attractive alternative to computing M realizations of (1) because statistical forecasts are obtained by evolving two rather than M spatial fields. However, such an approach presents a closure problem because the terms involving primed quantities in (4)–(5) are unknown. Formal moment closures were considered by Epstein (1969) and Fleming (1971) for the evolution of the mean field plus the full covariance tensor, but these rapidly become intractable as N becomes large. We consider instead the evolution of the mean Q_1 and variance Q_2 in the context of non-equilibrium statistical mechanics.

Central to our approach is the notion that nonlinear evolution according to (3) drives the p.d.f. p toward higher entropy (greater uncertainty or lower information content), as demonstrated for homogeneous dynamics by Carnevale, Frisch & Salmon (1981) and Carnevale & Holloway (1982). From information theory, entropy S is

related to p by

$$S = -\int p \ln p \, \mathrm{d}\boldsymbol{Y}, \tag{7}$$

where $\boldsymbol{Y}$ is a state vector in N-dimensional phase space. Given knowledge of second-order moments about the mean fields, the p.d.f. that maximizes S is joint-Gaussian, with

$$S = \tfrac{1}{2} \ln |\mathbf{C}| + \tfrac{1}{2} N(\ln 2\pi + 1), \tag{8}$$

where $\mathbf{C}$ is the N-dimensional correlation matrix (e.g. Carnevale *et al.* 1981; Stephenson & Doblas-Reyes 2000).

In the present context where we have knowledge of the mean Q_1 and of diagonal elements of $\mathbf{C}$ through the spatial variance field Q_2, the highest entropy p.d.f. is

$$p[q(\boldsymbol{x}, t)] = \frac{1}{(2\pi Q_2)^{1/2}} \exp\left[-\frac{(q - Q_1)^2}{2Q_2}\right], \tag{9}$$

and entropy is given by the integral $S = \int s \, \mathrm{d}\boldsymbol{x}$ of entropy density

$$s(\boldsymbol{x}, t) = -\int_{-\infty}^{\infty} p(q) \ln p(q) \, \mathrm{d}q = \tfrac{1}{2} \ln Q_2(\boldsymbol{x}, t) + \tfrac{1}{2}(\ln 2\pi + 1). \tag{10}$$

We seek a prediction scheme for Q_1 and Q_2 that drives S monotonically toward its highest attainable value. We also require consistency with the form and conservation properties of the exact moment equations (4)–(5).

We begin by rewriting the exact moment equations (4)–(5) as

$$\frac{\partial Q_1}{\partial t} = \underset{1\mathrm{A}'}{-\boldsymbol{u} \cdot \nabla Q_1} \underset{1\mathrm{B}'}{- \nabla \cdot \boldsymbol{T}^*} \tag{11}$$

$$\frac{\partial Q_2}{\partial t} = \underset{2\mathrm{A}'}{-\boldsymbol{u} \cdot \nabla Q_2} \underset{2\mathrm{B}'}{- 2\boldsymbol{T}^* \cdot \nabla Q_1} \underset{2\mathrm{C}'}{- \nabla \cdot \Sigma^*}, \tag{12}$$

where $\boldsymbol{u} = (u, v) = (-\Psi_y, \Psi_x)$ is mean velocity, $\boldsymbol{u}Q_1$ and $\boldsymbol{u}Q_2$ are reversible advective fluxes, and

$$\boldsymbol{T}^* = \overline{\boldsymbol{u}' q'}, \tag{13}$$

$$\boldsymbol{\Sigma}^* = \overline{\boldsymbol{u}' q'^2}, \tag{14}$$

are irreversible (entropy producing) fluxes, to be specified in terms of Q_1 and Q_2. Equations (11)–(12) also can be obtained via statistical mechanical arguments (e.g. McLennan 1989, Chap. 1).

Terms 1B′ and 2B′ containing irreversible flux $\boldsymbol{T}^*$ in (11)–(12) transfer variance between the mean and the disordered component, and conserve total variance $\int (Q_1^2 + Q_2) \, \mathrm{d}\boldsymbol{x}$. In addition, term 2B′ contains gradients of Q_1, indicating that uncertainty Q_2 tends to be produced most rapidly where such gradients are large. Term 2C′ involving irreversible flux $\boldsymbol{\Sigma}^*$ is conservative and hence redistributes uncertainty.

Following common practice in non-equilibrium thermodynamics, we can relate these fluxes linearly to gradients that vanish in equilibrium, so that

$$\boldsymbol{T}^* = -\eta \nabla (Q_1 - Q_1^*), \qquad \boldsymbol{\Sigma}^* = -\lambda \nabla (Q_1 - Q_1^*), \tag{15}$$

where Q_1^* and Q_2^* are equilibrium fields. Such equilibria can be calculated from equilibrium statistical mechanics (e.g. Salmon, Holloway & Hendershott 1976), as discussed further in § 5. For 'diffusion coefficients' η and λ in (15), we adopt a simple mixing-length form consisting of a length scale L times a characteristic velocity

$U \sim LQ_2^{1/2}$, each associated with the uncertain component of motion. Length scale L is specified as an eddy length scale of the uncertain component,

$$L = C_L(\mathscr{E}/\mathscr{Q})^{1/2}, \tag{16}$$

where C_L is an $O(1)$ constant,

$$\mathscr{Q} = \int Q_2 \, \mathrm{d}\boldsymbol{x} \tag{17}$$

is the spatially integrated variance of potential vorticity, and

$$\mathscr{E} = \int \overline{|\nabla\psi'|^2} \, \mathrm{d}\boldsymbol{x} = E - \int |\nabla\Psi|^2 \, \mathrm{d}\boldsymbol{x} \tag{18}$$

is the energy of the uncertain component, where total mean energy $E = \int |\nabla\psi^2| \, \mathrm{d}\boldsymbol{x}$ is determined from the initial conditions.

The above functional forms for $\boldsymbol{T}^*$ and $\boldsymbol{\Sigma}^*$ are always finite away from equilibrium. However, in ensembles having random initial errors, the correlations (13)–(14) initially vanish and must develop during an adjustment phase that is akin to 'aging to hydrodynamics' in microscopic systems (e.g. McLennan 1989). Information about this process can be obtained from evolution equations for the correlations. To construct such an equation for $\overline{\boldsymbol{u}'q'}$, we substract (4) from (1) to obtain $\partial q_i'/\partial t$ and treat similarly the Euler equation

$$\frac{\partial \boldsymbol{u}}{\partial t} = -\boldsymbol{u}\cdot\nabla\boldsymbol{u} - \frac{\nabla p}{\rho}, \tag{19}$$

where p is pressure and ρ is density, to obtain an equation for $\partial \boldsymbol{u}_i'/\partial t$. Multiplying these expressions by $\boldsymbol{u}_i'$ and q_i' respectively and ensemble averaging yields

$$\begin{aligned}\frac{\partial}{\partial t}\overline{\boldsymbol{u}'q'} &= \overline{\boldsymbol{u}'\frac{\partial q'}{\partial t}} + \overline{q'\frac{\partial \boldsymbol{u}'}{\partial t}} \\ &= -\bar{\boldsymbol{u}}\cdot\nabla(\overline{\boldsymbol{u}'q'}) - \overline{\boldsymbol{u}'(\boldsymbol{u}'\cdot\nabla)}Q_1 - \overline{q'(\boldsymbol{u}'\cdot\nabla)}\bar{\boldsymbol{u}} - \overline{\boldsymbol{u}'\cdot\nabla(\boldsymbol{u}'q')} - \frac{\overline{q'\nabla p'}}{\rho}.\end{aligned} \tag{20}$$

If initial errors are random, all averages on the right-hand side of the bottom line of (20) vanish except those in the second and fifth terms. (This has been verified numerically for the explicit ensembles of § 5.) The effect of the fifth term is difficult to characterize analytically, but numerically we have found that it largely correlates with the second term and is smaller in magnitude. Therefore we approximate the initial growth of $\overline{\boldsymbol{u}'q'}$ as that due to the second term in (20):

$$\frac{\partial}{\partial t}\overline{\boldsymbol{u}'q'} \approx \begin{pmatrix} \overline{u'^2}Q_{1x} + \overline{u'v'}Q_{1y} \\ \overline{u'v'}Q_{1x} + \overline{v'^2}Q_{1y} \end{pmatrix}. \tag{21}$$

If initial velocity errors are directed randomly, $\overline{u'v'} = 0$ and $\overline{u'^2} = \overline{v'^2} = U/2$, where $U \sim LQ_2^{1/2}$ is the characteristic error velocity as defined above. Thus

$$\overline{\boldsymbol{u}'q'} \equiv \boldsymbol{T}^* \sim \frac{L^2Q_2}{2}\nabla Q_1 t, \qquad t \lesssim Q_2^{-1/2}. \tag{22}$$

We suppose that following initial growth given by (22), $\boldsymbol{T}^*$ exponentially converges to (15) with $\eta = LQ_2^{1/2}$ according to

$$\boldsymbol{T}^* = L^2Q_2^{1/2}\gamma\nabla(Q_1 - \gamma Q_1^*), \tag{23}$$

where

$$\gamma(\boldsymbol{x},t) = 1 - \exp\left[-\int_0^t L^2(t')Q_2(\boldsymbol{x},t)\,\mathrm{d}t'/Q_2^{1/2}L^2\right]. \tag{24}$$

Application of similar arguments $\overline{\boldsymbol{u}'q'^2}$ yields

$$\boldsymbol{\Sigma}^* = L^2Q_2^{1/2}\gamma\nabla(Q_2 - \gamma Q_2^*). \tag{25}$$

The moment prediction equations then are given by (11)–(12), together with (16)–(18) and (23)–(25).

We now consider the evolution of entropy implied by these equations. Differentiating (10) with respect to time and substituting from (12), we have

$$\frac{\partial s}{\partial t} + \boldsymbol{u}\cdot\nabla s = -\frac{1}{2Q_2}(2\boldsymbol{T}^*\cdot\nabla Q_1 + \nabla\cdot\boldsymbol{\Sigma}^*). \tag{26}$$

Substituting forms (23) and (25) for irreversible fluxes $\boldsymbol{T}^*$ and $\boldsymbol{\Sigma}^*$ and integrating, we have entropy $S(t) = \int s(\boldsymbol{x},t)\,\mathrm{d}\boldsymbol{x}$ obeying

$$\frac{\mathrm{d}S}{\mathrm{d}t} = \int \gamma L^2Q_2^{1/2}\left[\frac{1}{Q_2}(|\nabla Q_1|^2 - \gamma\nabla Q_1\cdot\nabla Q_1^*) + \frac{1}{2}\frac{|\nabla Q_2|^2}{Q_2^2}\right]\mathrm{d}\boldsymbol{x}, \tag{27}$$

where we have used $\nabla Q_2^* = 0$ for the quasi-geostrophic systems considered here (Salmon *et al.* 1976). Equation (27) implies $\mathrm{d}S/\mathrm{d}t \geqslant 0$ when $Q_1^* = 0$, as when topography is absent, and in general at early times when γ is small. When Q_1^* is finite, a sufficient condition for $\mathrm{d}S/\mathrm{d}t \geqslant 0$ is that total uncertainty $\mathcal{Q}$, which evolves according to

$$\frac{\mathrm{d}\mathcal{Q}}{\mathrm{d}t} = \int \gamma L^2Q_2^{1/2}(|\nabla Q_1|^2 - \gamma\nabla Q_1\cdot\nabla Q_1^*)\,\mathrm{d}\boldsymbol{x}, \tag{28}$$

likewise increases. Such a monotonic increase in $\mathcal{Q}$ is anticipated in forecast scenarios in which observations constrain initial uncertainty, so that $\mathcal{Q} < \mathcal{Q}^*$ initially. Although the universality of such behaviour is not obvious from (28), we were unable to construct counter-examples, and for all of the forecast scenarios considered here $\mathrm{d}S/\mathrm{d}t \geqslant 0$, as reported in § 5.

4. Relation to turbulence closures and subgrid-scale parameterizations

The purpose of the method developed above is to predict evolving ensemble mean fields and uncertainties about those means. The method is relatively simple in that it involves quantities only at a single point in space. This is in contrast to the stochastic dynamic methods mentioned previously, as well as the direct interaction approximation (DIA) and eddy-damped quasi-normal Markovian (EDQNM) method, which predict correlations between flow variables at two points in space (e.g. Orszag 1977). Because of their complexity, the latter methods are most often formulated spectrally for ensembles that are homogeneous and isotropic, implying zero ensemble mean. Such theories have been considered as bases for subgrid-scale parameterization in atmospheric circulation models, for which spectral formulations are common (Frederiksen & Davies 1997). However, we have sought a spatial formulation that has straight-forward application to the irregular domains encountered in ocean models, and wish to consider non-zero ensemble means. Application of the DIA or an EDQNM scheme in such a context is formidably complex compared to the scheme developed here.

The approximations (23)–(25) to the irreversible fluxes resemble the BGK or relaxation-time approximation to the Boltzmann equation (Bhatnagar, Gross & Krook 1954; Chapman & Cowling 1970) in that nonlinear interactions are characterized as driving relaxation toward equilibrium at typical interaction timescales. In the case of the BGK approximation, relaxation is toward a Maxwellian p.d.f. characterized by local values of temperature and bulk velocity, and nearness to local equilibrium is assumed. In the present case, a purely local formulation is inappropriate because there exists no scale separation between interacting elements (eddies) and resolved scales of flow. As formulated here, our prediction equations thus relax local flow statistics toward global equilibrium values at rates determined by local magnitudes of uncertainty.

Other single-point schemes have been developed that predict spatial distributions of potential vorticity. That of Grote & Majda (2000) considers the evolution of single realizations subject to dissipation and random impulsive forcing. The predictions consist of sequences of equilibrium states having minumum enstrophy given the current energy. These equilibria are steady (Carnevale & Frederiksen 1987) and attract barotropic flows in which small-scale dissipation causes enstrophy but not energy to decay (Bretherton & Haidvogel 1976).

Another class of methods consists of subgrid-scale parameterizations that predict large-scale motion in the absence of information about the small scales. In the context of the barotropic vorticity equation, one such parameterization asserts downgradient eddy diffusion of q (e.g. Green 1970; Rhines & Young 1982). This approach has been used recently to predict mean circulation subject to forcing and dissipation in a flat-bottomed basin (Greatbach & Nadiga 2000). Alternatively, eddies have been assumed to drive resolved flows toward higher entropy (e.g. Merryfield & Holloway 1997).

Neither the Grote & Majda (2000) scheme nor the subgrid-scale parameterizations discussed above provide estimates of uncertainty. One subgrid-scale parameterization that does provide such an estimate is that of Kazantsev, Sommeria & Verron (1998, referred to herein as KSV). The KSV scheme specifies subgrid-scale eddy fluxes by maximizing the local rate of entropy production. The scheme can be formulated to predict first and second moments, much as here. However, there are at least two differences between the KSV scheme and the moment equations formulated in § 3. First, the KSV scheme restricts fluctuations to unresolved scales that have little energy, so that resolved mean-flow energy is conserved in the absence of forcing and dissipation. This energy conservation principle appears as a constraint in the variational problem (KSV, eq. (3.13)) that determines the eddy fluxes. In the prediction scenario considered here, however, fluctuations occur at all scales, and mean-flow energy hence is not conserved. (In instances where $Q_1^* = 0$, for example, mean-flow energy eventually vanishes.) Relaxing the energy conservation constraint in the KSV formulation removes terms containing the corresponding Lagrange multiplier b from KSV's moment equations (3.21)–(3.22). The remaining terms resemble our equations (11)–(12), (23) and (25) except that the irreversible terms now drive the moments toward uniformity rather than equilibria, the equilibration tendency having been lost in the removal of terms proportional to b.

A second difference between KSV and the present scheme is that the KSV diffusion coefficient A_E is simply proportional to local uncertainty (KSV, eq. (3.19)). The initial adjustment period over which correlations (13)–(14) develop thus is not accounted for, as it is here in equations (23)–(25). This adjustment plays a significant role in the early evolution of ensembles, as we demonstrate below.

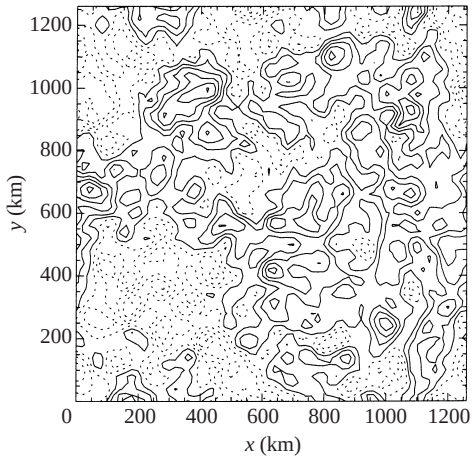

FIGURE 1. Topography for cases A, C and E. Solid contours denote regions shallower than the mean depth of 5000 m, and dashed contours regions that are deeper. Contour interval is 100 m.

5. Numerical tests

The skill of the prediction scheme developed in § 3 is now assessed in numerical tests. Forecast skill is compared to that of explicit ensemble solutions to (1) containing from 1 to 10^3 realizations. Estimates of 'true' moment evolution are provided by ensembles containing 10^4 realizations.

The system that we consider is intended as a simple model of an oceanic eddy field. It consists of a doubly periodic f-plane 1280 km on a side, overlying randomly generated topography (figure 1). Ensemble initial conditions are obtained by selecting a particular random velocity field, to which are added different random perturbations for each realization. The initial r.m.s. velocity in individual realizations is $10\,\mathrm{cm\,s^{-1}}$. Initial values of Q_1 and Q_2 are obtained by evaluating (2)–(3) for the 10^4 member ensembles. Details of the numerical scheme are summarized in the Appendix.

Moment prediction equations (11)–(12), (16)–(18) and (23)–(25) require specification of equilibrium moment fields Q_1^* and Q_2^*. According to Salmon *et al.* (1976), for the simple quasi-geostrophic systems considered here Q_1^* and Q_2^* are given by

$$\left(1 - \frac{b}{a}\nabla^2\right) Q_1^* = h, \qquad Q_2^* = [\overline{q(\boldsymbol{x})q(\boldsymbol{x}')}]^*_{\boldsymbol{x}'=\boldsymbol{x}}, \tag{29}$$

where

$$(b - a\nabla^{-2})[\overline{q(\boldsymbol{x})q(\boldsymbol{x}')}]^* = \delta(\boldsymbol{x} - \boldsymbol{x}') \tag{30}$$

(Salmon 1982). In (29)–(30), a and b are Lagrange multipliers that depend on the energy and potential enstrophy of the individual realizations as described in Carnevale & Frederiksen (1987). Values for a and b obtained via Newton–Raphson iteration are listed in table 1.

The equilibria described by (29)–(30) apply to inviscid quasi-geostrophic systems in which the equation of motion is truncated at some finite cutoff wavenumber, and depend on the cutoff wavenumber selected. These equilibria describe the long-time statistics of ensembles of numerical solutions to (1), in which a cutoff is necessarily employed (Merryfield & Holloway 1996). This choice of equilibrium is appropriate

Case	Grid resolution (km)	$(H_0 - H)_{\text{r.m.s.}}$ (m)	Initial error specification	a ($s^2\,cm^{-2}$)	b (s^2)
A	20	210	(A1), $k_c = 15k_f$	3.03	7.10×10^{13}
B	10	210	(A1), $k_c = 15k_f$	4.66	1.96×10^{14}
C	20	210	(A2)	3.14	6.34×10^{13}
D	20	0	(A1), $k_c = 15k_f$	−0.20	1.30×10^{14}
E	20	210	(A1), $k_c = 60k_f$	3.81	7.11×10^{13}

TABLE 1. Summary of cases A–E.

in the present study, in which we predict statistics of solutions to (1) given imperfect knowledge of initial conditions.

We proceed to describe five sets of experiments, summarized in table 1, in which we compare eight-month forecasts obtained from the moment equations of § 3 and from ensembles. Case A, the central experiment, uses a 20 km grid and has initial errors concentrated on small spatial scales. In case B the grid spacing is halved to 10 km. In case C the initial relative error is independent of scale, and in case D topographic variation is absent. In case E the magnitude of initial errors is much smaller than in the other cases.

5.1. *Case A: central experiment*

In this subsection, we first examine the 'true' evolution of Q_1 and Q_2 as deduced from an $M = 10^4$ ensemble. We then evaluate the performance of the moment prediction scheme, first by considering the ability of the irreversible terms in (11)–(12) to represent corresponding terms in the exact moment equations (4)–(5), and then by comparing the 'true' Q_1 and Q_2 with forecasts obtained from the moment equations (11)–(12) and from various sizes of sub-ensembles.

5.1.1. *'True' moment evolution*

The left-hand panels of figure 2 show 'true' $Q_1(\boldsymbol{x}, t)$ deduced from an $M = 10^4$ ensemble. Evolution is from an initial state uncorrelated with the equilibrium mean Ψ^* (figure 2*a*), toward Ψ^* (figure 2*c*, *e*, *g*). The corresponding decay of $\Psi - \Psi^*$ is illustrated in the right-hand panels of figure 2.

Figure 3 shows the evolution of uncertainty $Q_2(\boldsymbol{x}, t)$ as deduced from an $M = 10^4$ ensemble using (3). Because of the manner in which the initial error field is specified, Q_2 is initially uniform except for statistical noise (figure 3*a*). As the ensemble evolves, Q_2 develops strong intermittent peaks (figure 3*b*), much as in experiments of Lilly (1972) and Baumhefner & Julian (1972) involving two-member ensembles. These peaks broaden and disperse as overall uncertainty increases (figure 3*c*). Finally, Q_2 approaches its equilibrium form (figure 3*d*), which in this case is uniform (Salmon *et al.* 1976).

5.1.2. *Skill of irreversible terms in moment equations*

In evaluating the performance of the moment prediction scheme for case A, we consider first the ability of the irreversible flux terms in (11)–(12) to represent corresponding terms in the exact moment equations (4)–(5). We evaluate both sets of terms from the $M = 10^4$ ensemble. Figure 4 compares grid-point values of exact term 1B (horizontal axis) and its parameterization 1B′ with $C_L = 0.4$ (vertical axis), which drive Q_1 toward its equilibrium form. A perfect parameterization would place

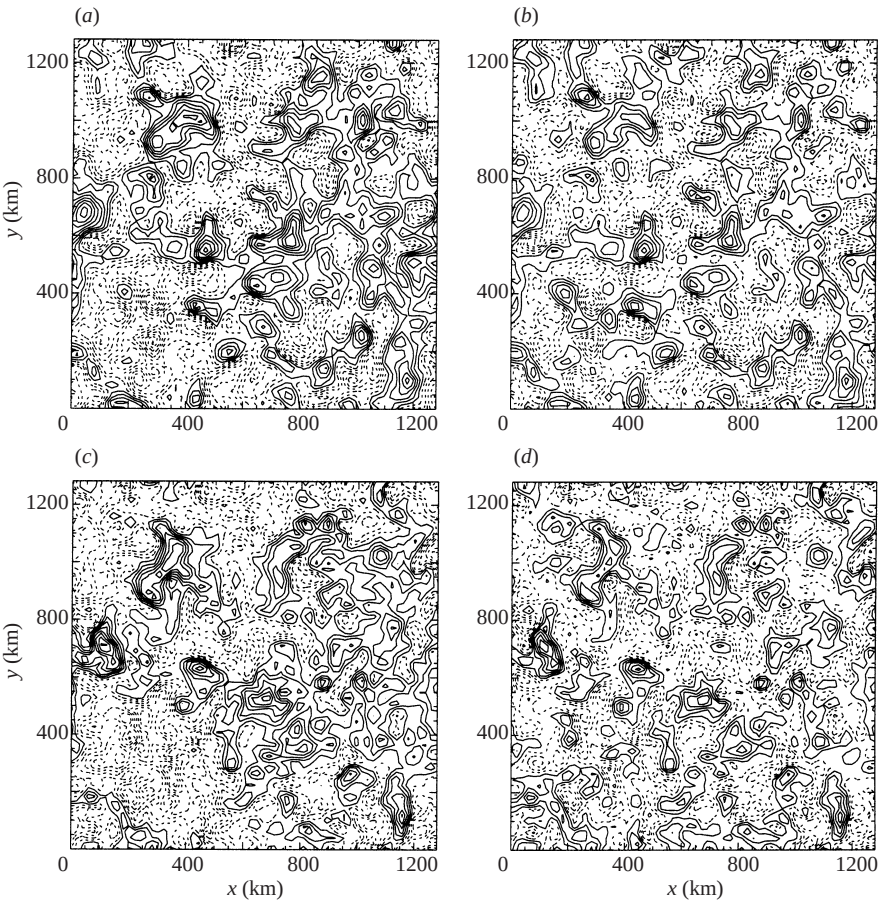

FIGURE 2 (*a–d*). For caption see facing page.

all points on the dashed lines having unit slope. At $t = 0.5$ months (figure 4*a*), explicit 1B and parameterization 1B′ are strongly linearly correlated with approximately correct slope. At $t = 2$ months (figure 4*b*) the correlation remains strong, with 1B′ underestimating slightly the magnitude of 1B. At $t = 8$ months (figure 4*c*), the temporal evolution of Q_1 has largely ceased (figure 2*g*, *h*), and the relation between 1B and 1B′ is dominated by statistical noise.

Figure 5 compares explicitly evaluated 2B in (5) with its parameterization 2B′ in (12). These terms irreversibly generate net uncertainty $\int Q_2 \, \mathrm{d}\boldsymbol{x}$. At $t = 0.5$ months (figure 5*a*), explicit 2B and its parameterization are strongly linearly correlated, with 2B′ tending to overestimate slightly the rate of uncertainty production. At $t = 2$ months (figure 5*b*) the correlation remains strong, with a slight tendency toward underestimation. At $t = 8$ months (figure 5*c*), uncertainty production has nearly ceased (figure 3*d*), and any relation between 2B and 2B′ is obscured by statistical noise.

Figure 6 similarly compares explicitly evaluated 2C in (5) with its parameterization 2C′ in (12). These terms drive Q_2 toward spatially uniform Q_2^*. At $t = 0.5$ months 2C and 2C′ are strongly correlated with approximately the correct slope. At $t = 2$ months the correlation has decayed somewhat, but the slope remains approximately

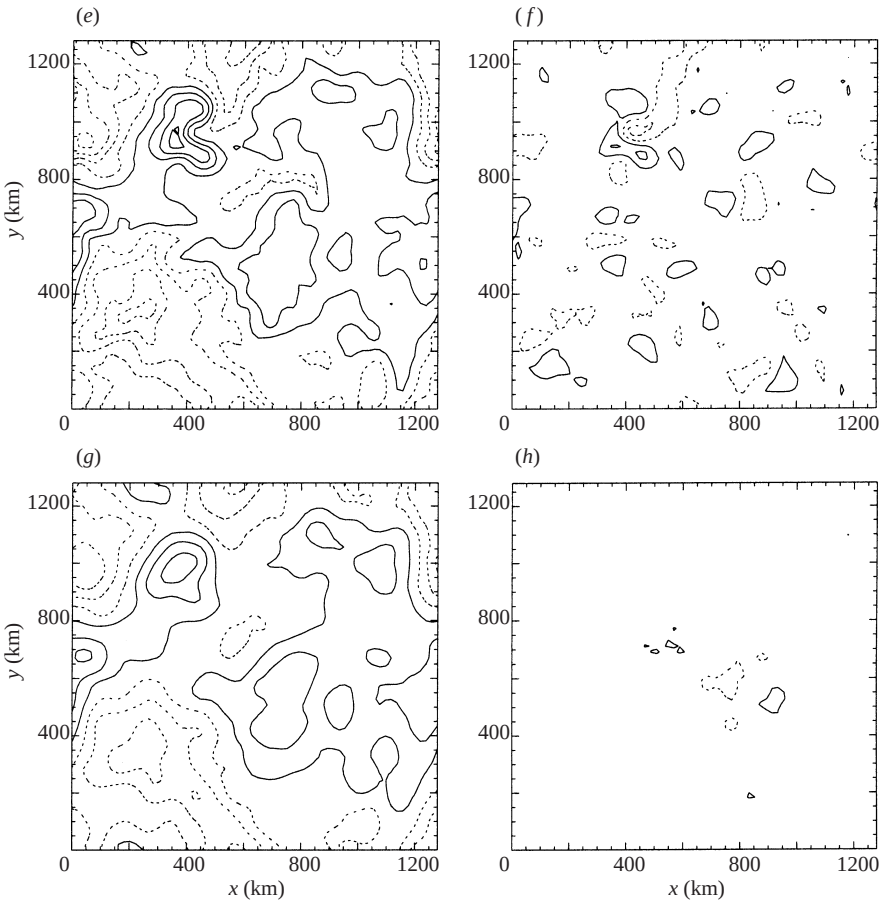

FIGURE 2. 'True' mean potential vorticity Q_1 (left-hand panels) and departures from equilibrium $Q_1 - Q_1^*$ (right-hand panels) for case A, as determined from an $M = 10^4$ ensemble. (a, b) $t = 0$; (c, d) $t = 0.5$ months; (e, f) $t = 2$ months; and (g, h) $t = 8$ months. Contour interval is $1.76 \times 10^{-6}\,\mathrm{s}^{-1}$ in panels $(a$–$g)$ $0.44 \times 10^{-6}\,\mathrm{s}^{-1}$ in panel (h).

correct. After 8 months (figure 6*c*) Q_2 is nearly featureless (figure 3*d*), and the relation between 2C and 2C′ is dominated by noise.

These results indicate that the irreversible flux terms in (11)–(12) represent the unknown terms in exact moment equations (4)–(5) with significant skill.

5.1.3. *Skill of moment forecasts*

The skill of moment prediction equations (11)–(12) in forecasting Q_1 and Q_2 is now compared to that of ensembles containing from $M = 1$ to 10^3 realizations, using an $M = 10^4$ ensemble as the 'truth'. The example in figure 7 shows mean Q_1 (thick curves) and confidence limits $Q_1 \pm Q_2^{1/2}$ (shaded intervals) for $y = 1040$ km and $t = 0.5$ months.

Because the moments evolve toward equilibrium fields Q_1^* and Q_2^*, we evaluate the skill in predicting departures from equilibrium. Two skill measures are employed. The first, Σ_M, measures accuracy in predicting the magnitude of these departures $Q_n - Q_n^*$

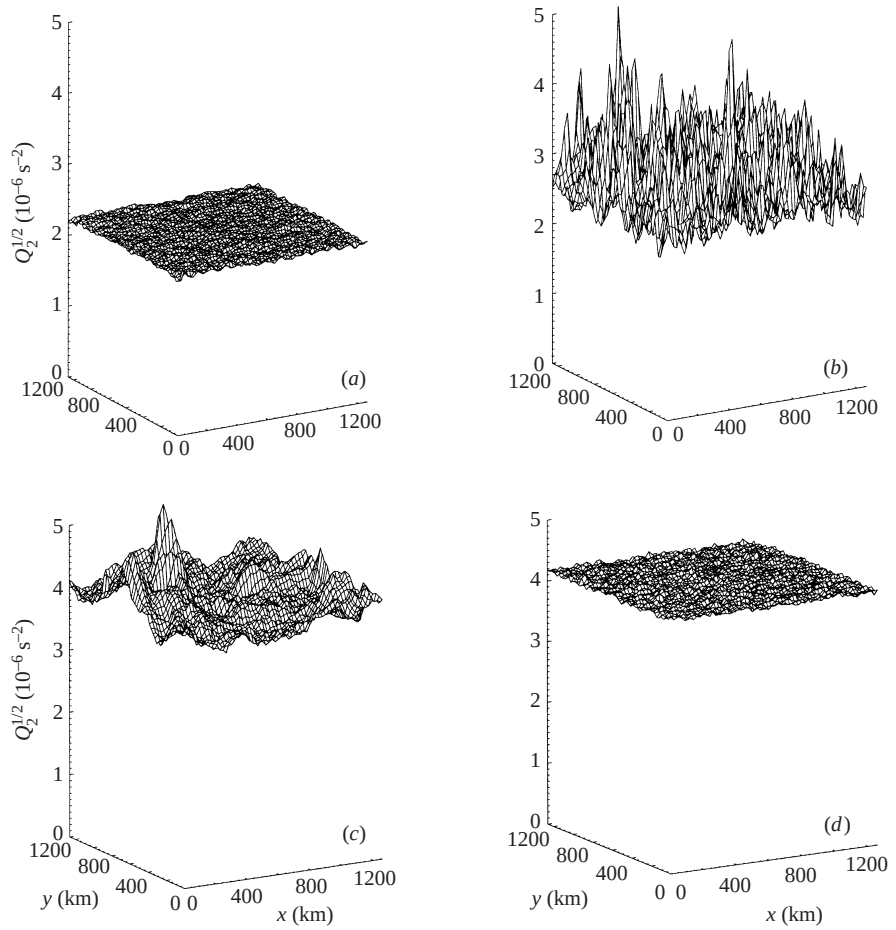

FIGURE 3. Square root $Q_2^{1/2}$ of the 'true' uncertainty field for case A. (*a*) $t = 0$; (*b*) $t = 0.5$ months; (*c*) $t = 2$ months; (*d*) $t = 8$ months.

($n = 1, 2$), and consists of the ratio of forecast to 'true' r.m.s. $Q_n - Q_n^*$:

$$\Sigma_M = \left[\frac{\int \text{forecast}\,(Q_n - Q_n^*)^2 \,\mathrm{d}\boldsymbol{x}}{\int \text{true}\,(Q_n - Q_n^*)^2 \,\mathrm{d}\boldsymbol{x}} \right]^{1/2} . \tag{31}$$

The second skill measure Σ_P gauges accuracy in predicting the spatial pattern of $Q_n - Q_n^*$, and consists of the spatial correlation coefficient of forecast and 'true' $Q_n - Q_n^*$:

$$\Sigma_P = \frac{\int [\text{forecast}\,(Q_n - Q_n^*)][\text{true}\,(Q_n - Q_n^*)] \,\mathrm{d}\boldsymbol{x}}{\left[\int \text{forecast}\,(Q_n - Q_n^*)^2 \,\mathrm{d}\boldsymbol{x}\right]^{1/2} \left[\int \text{true}\,(Q_n - Q_n^*)^2 \,\mathrm{d}\boldsymbol{x}\right]^{1/2}}. \tag{32}$$

A perfect forecast yields unit values in both cases.

Figure 8 illustrates the evolution of Σ_M and Σ_P for $Q_1 - Q_1^*$ and $Q_2 - Q_2^*$. Heavy solid

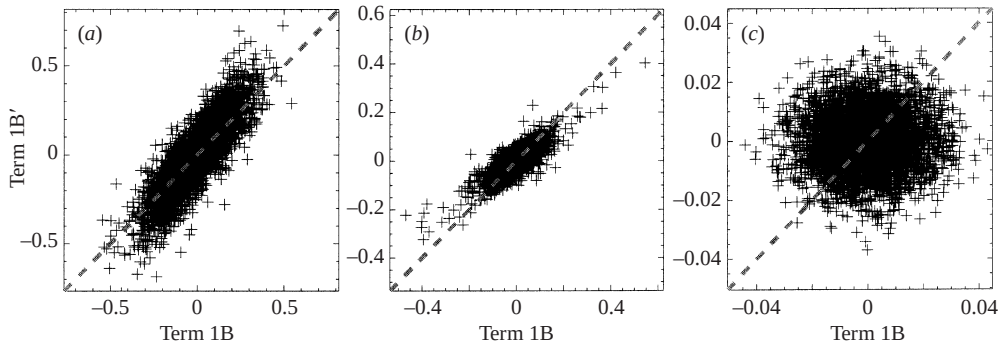

FIGURE 4. Pointwise values of term 1B in exact moment equation (4) (horizontal axis), versus its parameterization 1B′ in (11) (vertical axis), at (*a*) $t = 0.5$ months; (*b*) $t = 2$ months; (*c*) $t = 8$ months. The dashed lines indicate unit slope.

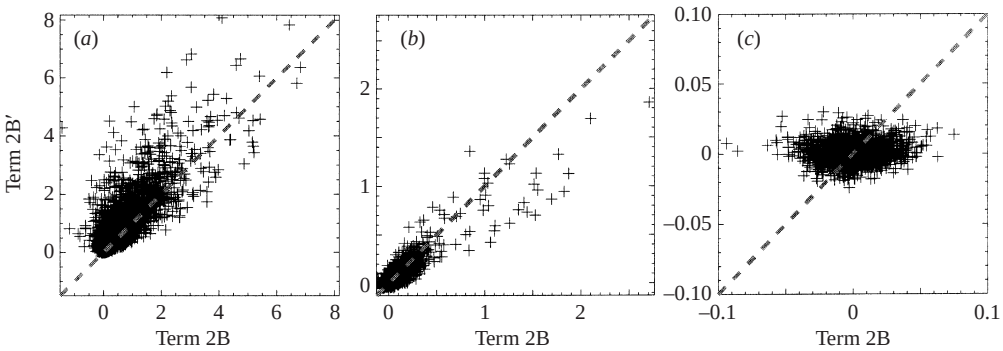

FIGURE 5. As in figure 4, but for term 2B in exact moment equation (5) (horizontal axis), versus its parameterization 2B′ in (12) (vertical axis).

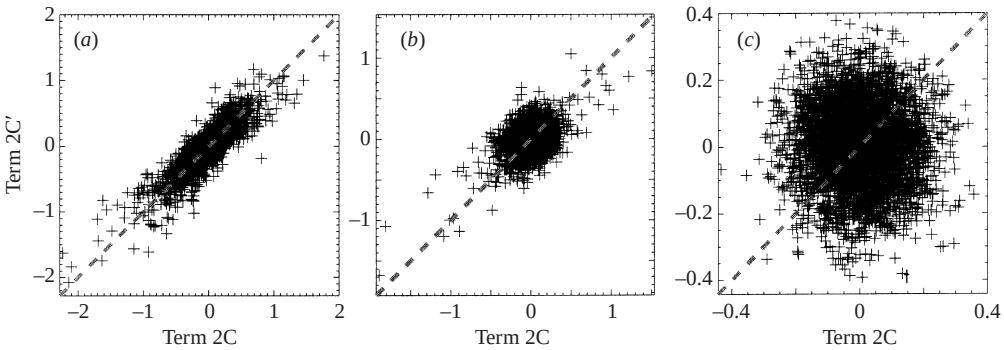

FIGURE 6. As in figure 4, but for term 2C in exact moment equation (5) (horizontal axis), versus its parameterization 2C′ in (12) (vertical axis).

curves represent a moment equation forecast having $C_L = 0.4$. For comparison, the thin solid curves represent a moment equation forecast having $C_L = 0.5$. The dashed curves, from thickest to thinnest, represent ensemble forecasts having $M = 10^3, 10^2, 10$ and 1. Unit values produced by perfect forecasts are indicated by the dotted lines.

According to figure 8(*a*), r.m.s. $Q_1 - Q_1^*$ from the moment equation forecast remains within 50% or so of its true value for the duration of the forecast. By contrast, the

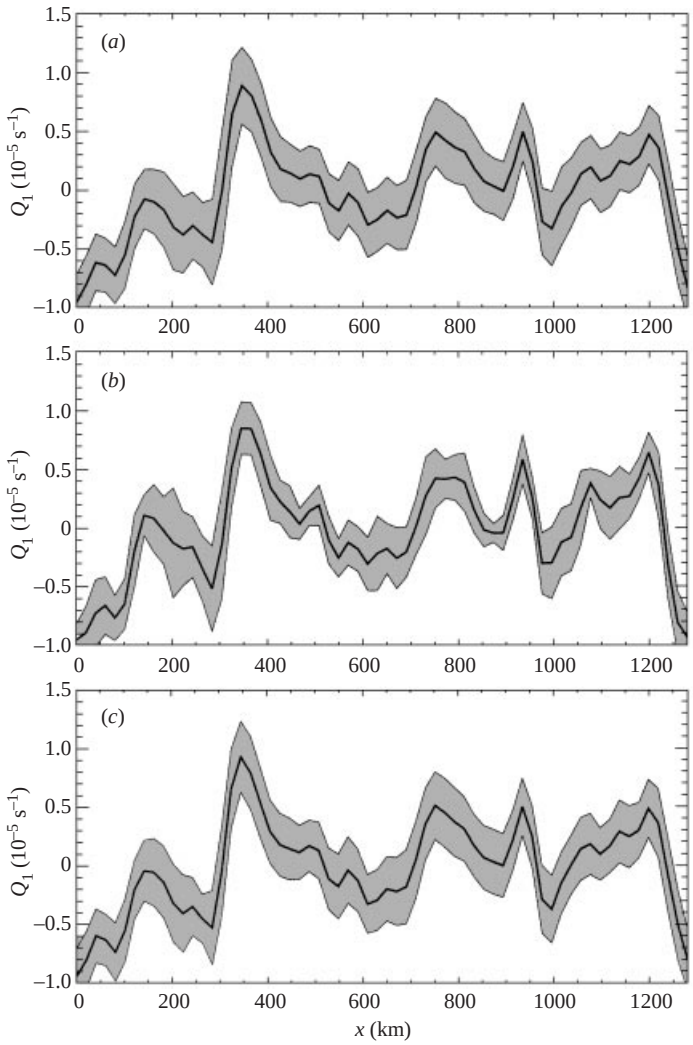

FIGURE 7. Mean potential vorticity Q_1 (thick curves) and confidence interval $Q_1 \pm Q_2^{1/2}$ (shaded intervals) at $y = 1040$ km, $t = 0.5$ months, for (a) $M = 10^4$ 'truth'; (b) $M = 10$ ensemble; (c) moment forecast with $C_L = 0.4$.

ensemble forecasts overestimate r.m.s. $Q_1 - Q_1^*$ with increasing severity as the ensemble size decreases. This is attributable in part to random statistical errors associated with finite ensemble size, which scale as $M^{-1/2}$.

Figure 8(b) shows that the spatial structure of $Q_1 - Q_1^*$ as predicted by the moment equation forecast is highly correlated with true $Q_1 - Q_1^*$ during the entire eight months. Skill measure Σ_P meets or exceeds that of ensembles having $M \leqslant 10^2$, and exceeds that of the $M = 10^3$ ensemble during the latter half of the forecast.

The skill in predictng r.m.s. $Q_2 - Q_2^*$ is shown in figure 8(c). For $t \gtrsim 1$ month, the moment equation forecast overestimates r.m.s. $Q_2 - Q_2^*$ by as much as a factor of four. However, ensembles having $M \leqslant 10^2$ fare even worse, and error in the $M = 10^3$ ensemble has grown nearly to this level by the end of the forecast. As for $Q_1 - Q_1^*$, ensemble forecast errors are at least partially attributable to random statistical errrors that prevent $Q_n - Q_n^*$ from decaying to realistic levels.

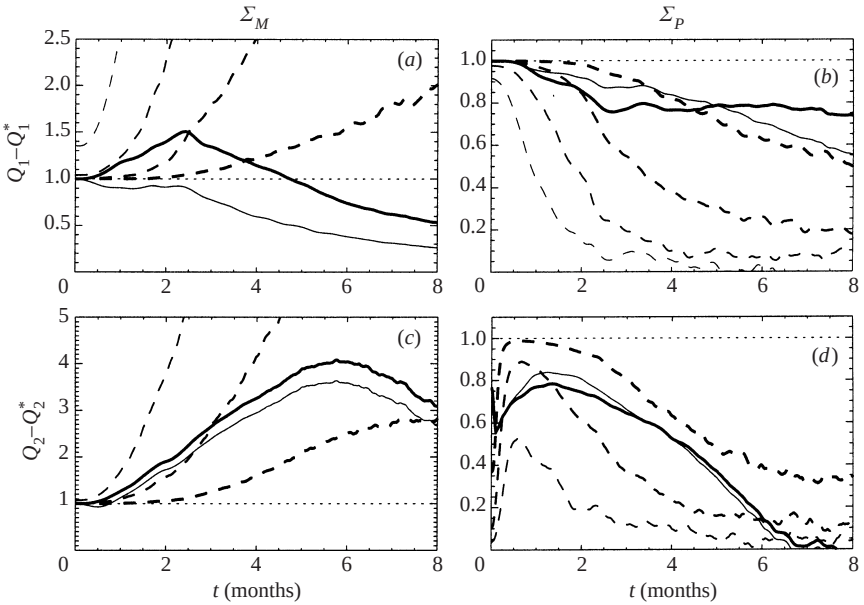

FIGURE 8. Evolution of forecast skill in case A for moment equation forecasts (thick solid curves, $C_L = 0.4$; thin solid curves, $C_L = 0.5$) and ensemble forecasts (dashed curves: from thickest to thinnest, $M = 10^3$, $M = 10^2$, $M = 10$, $M = 1$). Skill measures are Σ_M (left-hand panels), the ratio of predicted to true r.m.s. $Q_n - Q_n^*$ ($n = 1, 2$), and Σ_P (right-hand panels), the spatial correlation between predicted and true $Q_n - Q_n^*$. The $M = 1$ ensemble provides no forecast of $Q_2 - Q_2^*$.

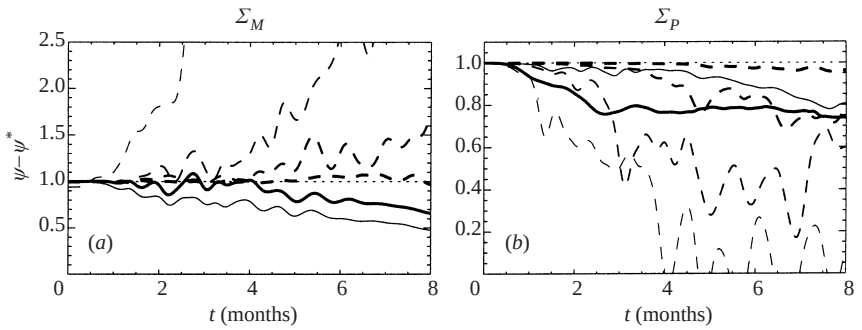

FIGURE 9. Evolution of skill in forecasting departures $\Psi - \Psi*$ from equilibrium for case A. The meaning of the different curves is as in figure 8.

Figure 8(d) shows the skill in predicting the spatial structure of $Q_2 - Q_2^*$, including the intermittent peaks in uncertainty seen in figure 3(b, c). The moment equation skill exceeds that of the $M \leqslant 10^2$ ensemble throughout much of the forecast.

In applying skill measures Σ_M and Σ_P to moments of the potential vorticity field, we measure primarily prediction skill for the small scales over which q characteristically varies (e.g. figure 2). Prediction skill for larger scales is assessed by applying Σ_M and Σ_P to departures from equilibrium $\Psi - \Psi^*$ of the mean streamfunction. The skill Σ_M in predicting r.m.s. $\Psi - \Psi^*$, shown in figure 9(a), is comparable to that of the $M = 10^2$ ensemble. The skill Σ_P in predicting the spatial structure of $\Psi - \Psi^*$ is comparable to that of the $M = 10^2$ ensemble only over the latter half of the forecast (figure 9b), although a prediction for which $C_L = 0.5$ (thin curve) fares somewhat better.

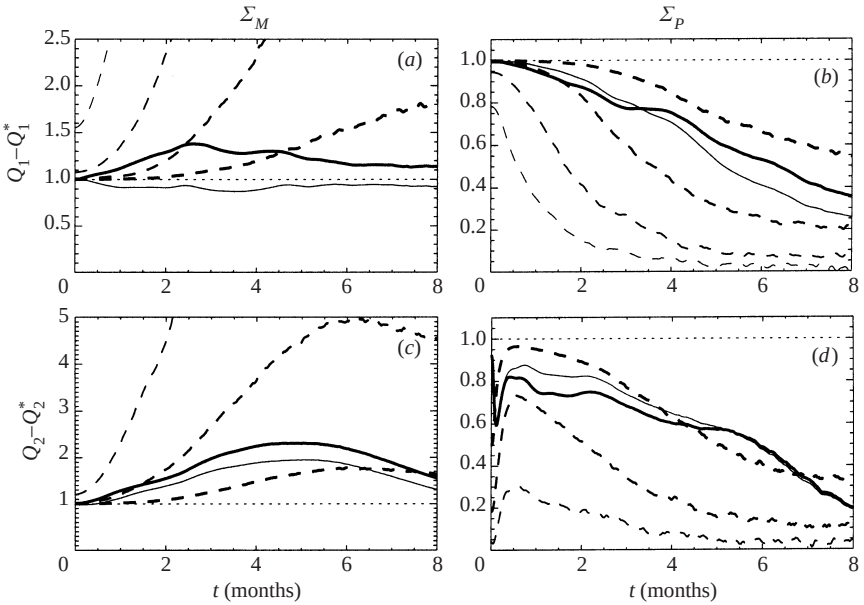

FIGURE 10. As for figure 8, but for high-resolution case B.

Overall, the skill of the moment equation forecast compares favourably with that of ensembles having $M \leqslant 10^2$. By some measures, the skill exceeds even that of the $M = 10^3$ ensemble late in the forecast.

5.2. *Case B: increased resolution*

Case B is similar to case A, except that spatial resolution is doubled. The performance in representing the magnitudes of $Q_n - Q_n^*$ (left-hand panels in figure 10) is comparable to that of the $M = 10^2$ ensemble at early times, and to that of the $M = 10^3$ ensemble at later times.

The skill of the moment equations in predicting the spatial structure of $Q_1 - Q_1^*$ lies between that of the $M = 10^2$ and $M = 10^3$ ensembles (figure 10*b*), and the skill in predicting spatial variations in uncertainty (figure 10*d*) is comparable, with correlation coefficient Σ_P exceeding 0.8 early in the forecast.

Overall, moment equation forecast skill exceeds that of an $M \leqslant 10^2$ ensemble and rivals that of an $M = 10^3$ ensemble.

5.3. *Case C: scale-independent initial relative error*

To test the generality of (11)–(12) we consider case C in which r.m.s. uncertainty in the initial fields is the same as in case A, but relative error $Q_2^{1/2}/Q_1$ is initially indepedent of spatial scale instead of concentrated at small sacles. In this case, the skill Σ_M in predicting the magnitudes of $Q_n - Q_n^*$ is generally comparable to case A (figure 11*a*, *c*) except during the first month or so. The skill Σ_P in predicting spatial patterns is weaker than in case A for $Q_1 - Q_1^*$ (figure 11*b*), but is stronger for $Q_2 - Q_2^*$ (figure 11*d*).

Except during the first month, the overall moment forecast skill exceeds that of the $M = 10^2$ ensemble, and in some respects rivals that of the $M = 10^3$ ensemble.

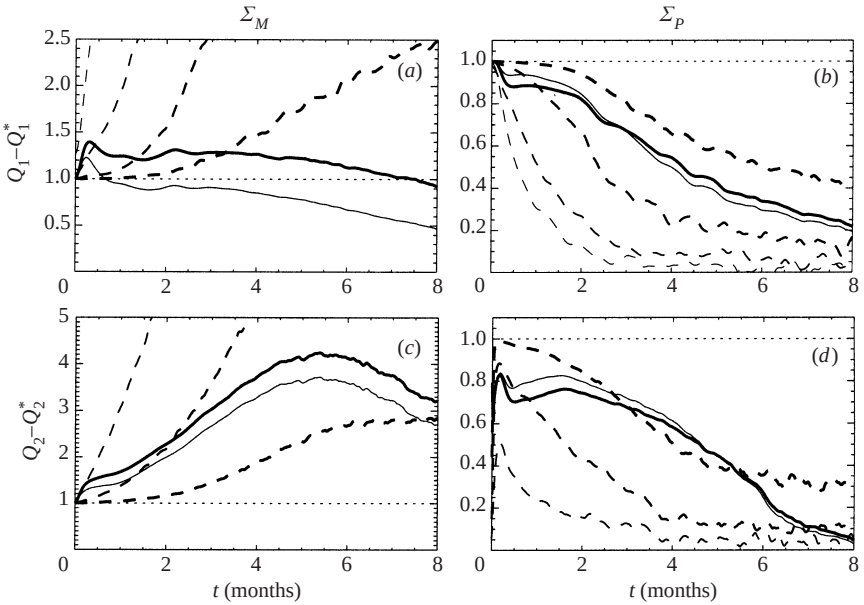

FIGURE 11. As for figure 8, but for case C having scale-independent relative initial error.

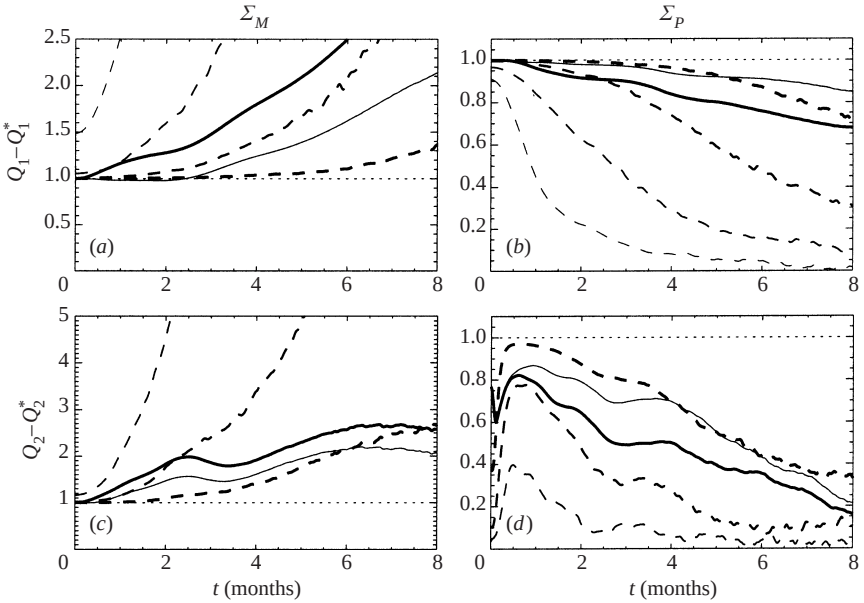

FIGURE 12. As for figure 8, but for no-topography case D.

5.4. *Case D: no topography*

Case D is identical to case A, except that topography is absent. In case D, the moment equation forecast systematically underestimates the decay of $Q_1 - Q_1^*$, as indicated by increasing Σ_M in figure 12(*a*). However, the spatial pattern of $Q_1 - Q_1^*$ is predicted with considerable skill (figure 12*b*).

The skill in predicting the magnitude of $Q_2 - Q_2^*$ (figure 12*c*) and its spatial pattern

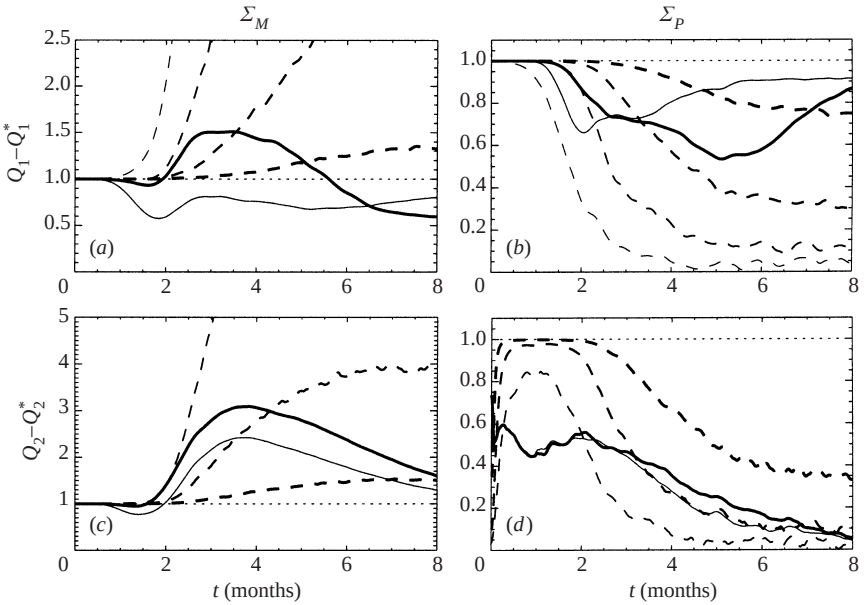

FIGURE 13. As for figure 8, but for small initial error case E.

(figure 12*d*) lies between that of $M = 10^2$ and $M = 10^3$ ensembles, and slightly exceeds that in case A.

5.5. *Case E: small initial errors*

Case E is similar to case A except that initial uncertainty is much smaller. This is accomplished by increasing the characteristic wavenumber k_c in the error spectrum from $15k_f$ to $60k_f$ (see Appendix). In this case, prediction of $Q_1 - Q_1^*$ is good at early times $t \lesssim 1$ month (as it is for ensembles) because the errors have not grown large enough to significantly affect evolution of the mean (figure 13). At intermediate times (1 month $\lesssim t \lesssim$ 3 months), the moment prediction is less skillful, faring at best as well as the $M = 10$ ensemble. At later times, skill measures lie between those of the $M = 10^2$ and the $M = 10^3$ ensemble.

Because initial uncertainty in case E is so small, the initial development of correlations (13)–(14) described by (24) is expected to play an especially significant role. Figure 14 shows the evolution of integrated uncertainty $\mathcal{Q} = \int Q_2 \, \mathrm{d}\boldsymbol{x}$ for case A (figure 14*a*) and for case E (figure 14*b*). Here 'true' $\mathcal{Q}$ is denoted by the solid curves and predicted $\mathcal{Q}$ by the dashed curves. To test sensitivity to our description (24) of correlation growth, we repeated the predictions replacing γ with unity in (23) and (25), in effect assuming that the development of correlations is instantaneous. These predictions are denoted by the dotted curves. In case A where initial errors are comparatively large, the initial adjustment is relatively rapid and the two predictions do not differ substantially (figure 14*a*). Nonetheless, the prediction that employs (24) succeeds in forecasting the relatively slow initial rate of error growth, whereas the prediction that neglects the adjustment process forecasts initial error growth that is too rapid. This effect is more dramatic in case E where initial errors are very small: here true error growth is almost nil until $t \gtrsim 1$ month (figure 14*b*). The prediction that employs (24) succeeds in forecasting this behaviour, and provides reasonable estimates of $\mathcal{Q}$ throughout the forecast. However, the prediction that neglects the adjustment process fails to predict the slow initial error growth.

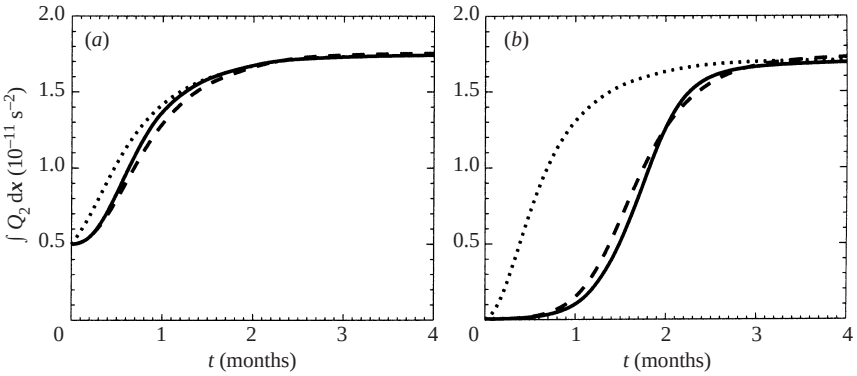

FIGURE 14. Evolution of spatially integrated uncertainty Q_2 for (*a*) case A; (*b*) case E having small initial uncertainty. Solid curves; 'truth'; dashed: moment forecast with initial development of correlations described by (24); dotted: moment forecasts assuming correlations develop instantaneously.

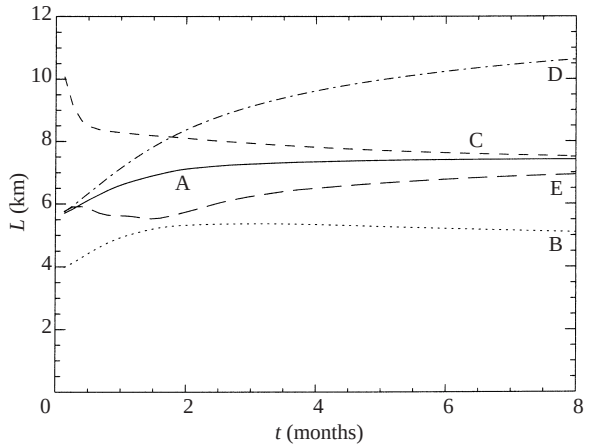

FIGURE 15. Evolution of uncertain component eddy length scale L in moment forecasts with $C_L = 0.4$, for cases A–E.

5.6. *Evolution of L and S*

Figure 15 shows the evolution of eddy length scale L of the uncertain component, which appears in (23)–(25). In case A (solid curve), L increases from less than 6 km at $t = 0$ to 7.5 km at $t = 8$ months. The relatively small initial value of L is consistent with the initial concentration of the uncertain component on small scales. In case B, L is smaller than in case A, reflecting the finer resolution of case B. In case C, L is initially larger than in case A, reflecting the presence of initial uncertainty at large as well as small scales. In case D, L initially is the same as in case A because initial conditions are similar. However, at later times L exceeds that in case A because equilibrium uncertainty in case D is concentrated at larger spatial scales.

Figure 16 shows the monotonic increase of entropy S for moment equation forecasts A–E. Entropy in case B is larger than in case A, in part because of the greater number of degrees of freedom. In case C, initial S is comparable to that in case A but grows more rapidly, apparently because the initial presence of uncertainty on large scales accelerates error growth relative to cases in which initial uncertainty is concentrated on small scales. Entropy in case D initially is the same as in case A, but grows toward

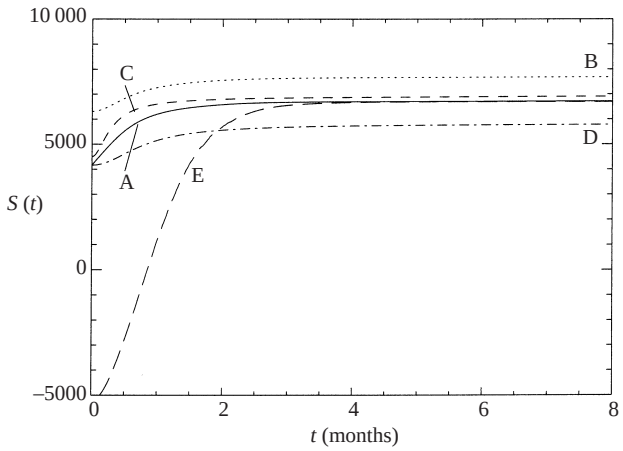

FIGURE 16. Evolution of entropy S according to moment equation forecasts with $C_L = 0.4$, for cases A–E. For high-resolution case B, $S/4$ is plotted so that each curve is proportional to entropy per degree of freedom.

a smaller equilibrium value. Entropy in case E is initially much lower than in the other cases due to the very small initial uncertainty.

6. Summary and discussion

Guided by non-equilibrium statistical mechanics, we predict the statistical evolution of inviscid quasi-geostrophic turbulence. Our method operates in the spatial domain and forecasts the first moment or mean Q_1 of potential vorticity, and the diagonal of the second moment or variance Q_2 about the mean. Thus we predict uncertainty and the feedback of the uncertain component upon the mean without performing ensemble forecasts. The method also represents the entropy gain or information loss that occurs as moments evolve from observationally constrained initial conditions.

Moment evolution equations that are consistent with exact moment equations (4)–(5) are obtained in terms of reversible (advective) and irreversible (entropy producing) fluxes. The irreversible fluxes are specified in terms of known moments, where we consider a simple specification based on mixing-length arguments and an approximate description of initial correlation growth. Using even this simple form, moment equation forecasts outperformed $M = 10^2$ ensemble forecasts and sometimes rivalled $M = 10^3$ ensembles in a range of numerical examples. Because the moment equations evolve just two spatial fields versus M spatial fields for ensembles, this performance is achieved at greatly reduced computational cost.

This paper focuses on the idealized case of inviscid unstratified quasi-geostrophic turbulence, and a challenge will be to apply this approach in a more realistic context. Real oceans and atmosphere are subject to forcing and dissipation, and terms representing these effects will arise in moment equations. As well, our moment forecast scheme requires specification of maximum entropy fields Q_n^* or approximations thereof. Progress in achieving more realistic Q_n^* is reported by Merryfield (1998) for stratified quasigeostrophic flows, and by Merryfield, Cummins & Holloway (2001) for unstratified flows, over finite topography. The moment prediction scheme in more realistic cases may also incorporate a spatially varying uncertain-component eddy length scale L, as well as anisotropic irreversible fluxes $\boldsymbol{T}$ and $\boldsymbol{\Sigma}$, especially where coastlines and steep topography constrain circulation.

This work was supported by the Office of Naval Research (N00014-99-1-0050).

Appendix. Details of numerical computations

In the case of ensemble calculations, equation (1) for each realization i was integrated using a pseudospectral scheme (e.g. Canuto *et al.* 1988), dealiased by the 2/3 rule. Temporal integration was via a leapfrog scheme, stablized by a Robert filter. Topography h was constructed by drawing complex spectral coefficients from a bi-normal distribution and scaling by $k^{-1/2}(k+4k_f)^{-5/4}$, where k is wavenumber and $k_f = 2\pi/1280\,\mathrm{km}$ is the fundamental wavenumber. Initial relative vorticities $\nabla^2\psi_i$, $i = 1 \ldots M$, consisted of a mean component $\nabla^2\Psi_0$ and error components $\nabla^2\psi'_{i0}$. The mean $\nabla^2\Psi_0$ was specified by again drawing Fourier coefficients from a bi-normal distribution, in this instance scaling by $k^{3/2}(k+5k_f)^{-3}$. In all instances except case C, errors $\nabla^2\psi'_{i0}$ were obtained by generating additional random realizations $\nabla^2\psi_i$ using the same scheme, and setting

$$(\nabla^2\psi'_{i0})_{\boldsymbol{k}} = [(\nabla^2\psi_i)_{\boldsymbol{k}} - (\nabla^2\Psi_0)_{\boldsymbol{k}}]F(k), \tag{A 1}$$

with $F(k) = \Delta + (1-\Delta)(1-\mathrm{e}^{(-k/k_c)^2})$, where Δ is a numerical constant set to 10^{-2}, and $k_c = 15k_f$ (cases A, B and D) or $k_c = 60k_f$ (case E). Prescription (A1) concentrates initial error at small spatial scales ($k \gtrsim k_c$). In case C, we alternatively prescribe equal relative initial error on all spatial scales,

$$(\nabla^2\psi'_{i0})_{\boldsymbol{k}} = [(\nabla^2\psi_i)_{\boldsymbol{k}}] - (\nabla^2\Psi_0)_{\boldsymbol{k}}]\Delta', \tag{A 2}$$

with $\Delta' = 0.473$, which gives case C the same initial error variance as cases A, B and D.

Moment forecast equations (11)–(12), (16)–(18) and (23)–(25) also were solved pseudospectrally, with initial conditions for Q_1 and Q_2 computed via (2)–(3) from 'true' $M = 10^4$ ensemble initial conditions.

REFERENCES

Baumhefner, D. P. & Julian, P. R. 1972 The reference level problem, its location and use in numerical weather prediction. *J. Atmos. Sci.* **29**, 285–299.

Bhatnagar, P. L., Gross, E. P. & Krook, M. 1954 Model for collision processes in gases, I. *Phys. Rev.* **94**, 511–524.

Bretherton, F. P. & Haidvogel, D. B. 1976 Two-dimensional turbulence above topography. *J. Fluid Mech.* **78**, 129–154.

Canuto, C., Hussaini, M. Y., Quarteroni, A. & Zang, T. A. 1988 *Spectral Methods in Fluid Mechanics.* Springer.

Carnevale, G. F. & Frederiksen, J. S. 1987 Nonlinear stability and statistical mechanics of flow over topography. *J. Fluid Mech.* **175**, 157–181.

Carnevale, G. F., Frisch, U. & Salmon, R. 1981 *H* theorems in statistical fluid dynamics. *J. Phys.* A **14**, 1701–1718.

Carnevale, G. F. & Holloway, G. 1982 Information decay and the predictability of turbulent flows. *J. Fluid Mech.* **116**, 115–121.

Chapman, S. & Cowling, T. G. 1970 *The Mathematical Theory of Non-Uniform Gases.* Cambridge University Press.

Epstein, E. S. 1969 Stochastic dynamic prediction. *Tellus* **21**, 739–759.

Fleming, R. J. 1971 On stochastic dynamics prediction. *Mon. Wea. Rev.* **99**, 851–872.

Frederiksen, J. S. & Davies, A. G. 1997 Eddy viscosity and stochastic backscatter parameterizations on the sphere for atmospheric circulation models. *J. Atmos. Sci.* **54**, 2475–2492.

Gleeson, T. A. 1970 Statistical-dynamical prediction. *J. Appl. Met.* **9**, 333–344.

Greatbach, R. J. & Nadiga, B. T. 2000 Four-gyre circulation in a barotropic model with double-gyre wind forcing. *J. Phys. Oceanogr.* **30**, 1461–1471.

Green, J. S. A. 1970 Transfer properties of the large-scale eddies and the general circulation of the atmosphere. *Q. J. R. Met. Soc.* **96**, 157–185.

Grote, M. J. & Majda, A. J. 2000 Crude closure for flow with topography through large scale statistical theory. *Nonlinearity* **13**, 569–600.

Houtekamer, P. L. & Derome, J. 1995 Methods for ensemble prediction. *Mon. Wea. Rev.* **123**, 2181–2196.

Kazantsev, E., Sommeria, J. & Verron, J. 1998 Subgrid-scale eddy parameterization by statistical mechanics in a barotropic ocean model. *J. Phys. Oceanogr.* **28**, 1017–1042 (referred to herein as KSV).

Khinchin, A. I. 1949 *Mathematical Foundations of Statistical Mechanics*. Dover.

Leith, C. A. 1974 Theoretical skill of Monte Carlo forecasts. *Mon. Wea. Rev.* **102**, 409–418.

Lilly, D. K. 1972 Numerical simulation studies of two-dimensional turbulence: II. Stability and predictability studies. *Geophys. Fluid Dyn.* **4**, 1–28.

McLennan, J. A. 1989 *Introduction to Nonequilibrium Statistical Mechanics*. Prentice-Hall.

Merryfield, W. J. 1998 Effects of stratification on quasi-geostrophic inviscid equilibria. *J. Fluid Mech.* **354**, 345–356.

Merryfield, W. J., Cummins, P. F. & Holloway, G. 2001 Equilibrium statistical mechanics of barotropic flow over finite topography. *J. Phys. Oceanogr.* **31**, 1880–1890.

Merryfield, W. J. & Holloway, G. 1996 Inviscid quasi-geostrophic flow over topography: testing statistical mechanical theory. *J. Fluid Mech.* **309**, 85–91.

Merryfield, W. J. & Holloway, G. 1997 Topographic stress parameterization in a quasi-geostrophic barotropic model. *J. Fluid Mech.* **341**, 1–18.

Orszag, S. A. 1977 Lectures on the statistical theory of turbulence. In *Fluid Dynamics* (ed. R. Balian & J.-L. Peube), pp. 235–374. Gordon & Breach.

Rhines, P. B. & Young, W. R. 1982 Homogenization of potential vorticity in planetary gyres. *J. Fluid Mech.* **122**, 327–347.

Salmon, R. 1982 Geostrophic turbulence. In *Topics in Ocean Physics, Proc. Intl School Phys. 'Enrico Fermi', Varenna, Italy*, pp. 30–78.

Salmon, R. 1998 *Lectures on Geophysical Fluid Dynamics*. Oxford University Press.

Salmon, R., Holloway, G. & Hendershott, M. C. 1976 The equilibrium statistical mechanics of simple quasi-geostrophic models. *J. Fluid Mech.* **75**, 691–703.

Shannon, C. E. & Weaver, W. 1949 *The Mathematical Theory of Communication*. University of Illinois Press.

Stephenson, D. B. & Doblas-Reyes, F. J. 2000 Statistical methods for interpreting Monte Carlo forecasts. *Tellus* **52**A, 300–322.